ADVANCED ENERGY MATERIALS
www.advenergymat.de

Templated N-Doped Carbon Nanospheres with Tailored Porosity for High Performance PEM Fuel Cell Catalysts Under a Wide Range of Conditions

Julian Martin, Sven Küspert, Kläre Christmann, Robert Marić, Miriam von Holst, Hassan Fadlullah, Patrick Elsässer, K. Andreas Friedrich, Severin Vierrath, Nada Zamel, and Anna Fischer**

Recent studies have shown the importance of porous carbon supports in achieving high-performance proton exchange membrane fuel cells (PEMFCs). Porous carbon supports control the cascaded oxygen and proton mass transport through the intraparticle porosity inside the electrocatalyst and through the interparticle porosity throughout the electrode. Here, two monodisperse mesoporous (10 and 28 nm pore size) N-doped carbon (MPNC) nanosphere supports with large particle sizes (>100 nm) are presented as supports for the design of advanced Pt-based PEMFC cathode electrocatalysts. The morphology and structure of the MPNC nanosphere supports and derived catalysts enable a 3D bottom-up design of the catalyst layer in terms of intra- and interparticle porosities, thereby positively impacting the fuel cell performance. Characterization at rotating disc electrode (RDE) and PEMFC single-cell level reveals the strong potential of the MPNC as catalyst support materials, combining excellent oxygen transport properties and improved mass activities. The MPNC-based catalysts achieve 0.66 W cm^{-2} at 0.76 V in single-cell configuration, outperforming state-of-the-art reference catalyst material by 27%. The results confirm not only the advantages of mesoporous N-doped carbons as advanced catalyst supports but also highlight the underexplored potential of tailoring performance determining parameters of the carbon support such as pore size and particle size.

1. Introduction

On the road to renewable energy systems, the recent resurgence of strong commercial interest in proton exchange membrane fuel cells (PEMFCs) as published in various national hydrogen strategies fueled extensive research in dedicated material science and engineering.[1] To reduce the cost of the fuel cell system and at the same time meet the stability standards for, e.g., the heavy-duty transportation sector, electrocatalyst, and catalyst layer design become crucial.[2] In this context, further optimization of the catalyst-coated membrane (CCM) and the membrane electrode assembly (MEA) structure offers substantial potential for additional improvements in mass transport and performance, despite significant advances already reported in the literature.[3] The carbon-supported Pt electrocatalyst is one important structure-directing building block guiding the CCM 3D porous structure. Here, mainly the structure of the

J. Martin, S. Küspert, P. Elsässer, A. Fischer
Institute of Inorganic and Analytical Chemistry (IAAC)
Inorganic Functional Materials and Nanomaterials
University of Freiburg
Albertstraße 21, 79104 Freiburg, Germany
E-mail: anna.fischer@ac.uni-freiburg.de

J. Martin, S. Küspert, P. Elsässer, S. Vierrath, A. Fischer
Freiburg Materials Research Center (FMF)
University of Freiburg
Stefan-Meier-Straße 21, 79104 Freiburg, Germany

The ORCID identification number(s) for the author(s) of this article can be found under https://doi.org/10.1002/aenm.202500954

DOI: 10.1002/aenm.202500954

K. Christmann, N. Zamel
Fraunhofer Institute for Solar Energy Systems (ISE)
Heidenhofstr. 2, 79110 Freiburg, Germany
E-mail: nada.zamel@ise.fraunhofer.de

R. Marić
Heraeus Precious Metals GmbH & Co. KG
Heraeusstrasse 12–14, 63450 Hanau, Germany

M. von Holst, H. Fadlullah, S. Vierrath
Hahn-Schickard-Gesellschaft für angewandte Forschung e.V.
Georges-Köhler-Allee 103, 79110 Freiburg, Germany

K. A. Friedrich
German Aerospace Center
Institute for Engineering Thermodynamics
Pfaffenwaldring 38–40, 70569 Stuttgart, Germany

K. A. Friedrich
Institute of Building Energetics
Thermal Engineering and Energy Storage (IGTE)
University of Stuttgart
Pfaffenwaldring 31, 70569 Stuttgart, Germany

carbon supports directs the packing and resulting porosity in the CCM (**Figure 1**). The importance of accessible pores in the carbon support for a low O_2 transport resistance and decreased catalyst poisoning was demonstrated.[4] Furthermore, the doping of carbon supports with nitrogen can favor an optimized ionomer coverage enabling increased mass transport.[5] Combining the concepts of N-doping and increased porosity, previous studies demonstrated high-performance oxygen reduction reaction (ORR) catalysts based on spherical, microporous, N-doped carbon supports, while the beneficial effect of tailored mesoporosity in mesoporous carbon-based electrocatalysts was also confirmed.[6,7] Regardless of the proven benefits of mesoporous carbons and the progress made in the field, there is still a lack of comprehensive understanding of their underlying performance-enhancing mechanisms, and the need for advanced in situ PEMFC characterization methods to reveal ionomer-related performance effects (such as ionomer distribution and blocked electrochemical active surface area (ECSA)) has become apparent. Hence methods such as CO displacement, CO stripping, and CO capacitance allow for gaining insights on the ionomer-carbon and ionomer-catalyst interplay and investigate the potential of tailored mesoporous carbon support materials for PEMFC electrode design.[8–10]

Herein, we present two monodisperse mesoporous N-doped carbon (MPNC) nanosphere supports with templated spherical pore sizes of 28 and 10 nm and particle sizes of 182 ± 22 nm and 115 ± 14 nm as advanced carbon supports for the design of 3D porous Pt-based ORR catalysts. These combine i) tailored intraparticle mesoporosity for optimized Pt accessibility, ii) N-doping for optimized ionomer-carbon interaction, iii) monodispersity for tailored interparticle porosity within the catalyst layer (CL) and CCM, and iv) large carbon support particle sizes (>100 nm) for fast mass transport throughout the CL/CCM thickness, resulting in a carbon support-based bottom-up CL/CCM/MEA structuring for improved PEMFC performance. To solely study the effect of the carbon supports and have a fair comparison to state-of-the-art carbon supports, Pt catalysts with nearly identical Pt (particle and crystallite) size distributions were deposited on both the MPNCs and the reference carbon support Ketjenblack EC-300J (KB), the latter having a primary particle size of 30–50 nm and meso- and micropores mainly smaller than 10 nm.[5,11]

The synthesized platinum-based electrocatalysts were thoroughly investigated in terms of their physicochemical performance-determining properties as well as by advanced fuel cell analysis techniques to elucidate structure-function correlations, namely the effect of the carbon support structure (i–iv) on ionomer distribution/coverage as well as on mass transport properties for an optimized overall fuel cell performance. With this approach, the tremendous potential for PEMFC performance optimization solely associated with advanced carbon support design could be demonstrated.

2. Mesoporous N-Doped Carbon Supports - Synthesis and Characterization

Monodisperse MPNC nanospheres were synthesized by hard-templating combining oxidative polymerization of aniline, monodisperse spherical SiO_2 nano templates, and colloidal self-assembly, as reported by us previously.[12–15] Carbonization (1000 °C under N_2 atmosphere) and template removal by etching yielded mesoporous MPNC nanospheres with interconnected spherical mesopores throughout the particles, as demonstrated by us previously by 3D STEM tomography.[15,16] By using monodisperse spherical SiO_2 nanotemplates with a size of 7 ± 2 nm and 23 ± 2 nm (as determined by scanning electron microscopy (SEM)), MPNC nanospheres with two different spherical mesopore pore sizes were obtained (MPNC7 and MPNC23, respectively). The MPNC nanospheres have a monodisperse particle size centered around 115 ± 14 nm and 182 ± 22 nm for MPNC7 and MPNC23, respectively (**Figure 2**a–c; Figure S1, Supporting Information), corresponding to an ultra-low polydispersity index of 1.05 (calculation based on the particle diameter dispersity and the IUPAC definition of polydispersity).[17] The tailored mesoporosity combined with the particles monodispersity qualifies the MPNC nanospheres as suitable model carbon supports for advanced catalyst and CCM design, thereby allowing to study and optimize morphology and porosity effects on PEMFC performance (Figure 1).

The porosity of the MPNC nanospheres was determined by N_2 physisorption (Figures S2–S4, Supporting Information) and compared with a commercially available, high surface area carbon support, namely Ketjenblack EC-300J (KB). The BET surface area of MPNC7, MPNC23, and KB accounted for 789, 603, and 785 $m^2\ g^{-1}$, respectively, in line with high surface area carbons. The type IV isotherm (characterized by a hysteresis) illustrates the predominantly mesoporous character of the MPNC materials, while only a small hysteresis is found for KB.[18] The pore size distribution of the MPNCs (determined by applying a quenched solid density function theory (QSDFT) model) reveals, in line with SEM and TEM results, accessible templated mesopores (with a maximum at 10 and 28 nm) and micropores for both MPNC7 and MPNC23, respectively.

The bulk chemical composition determined by elemental analysis (EA) shows a high degree of N-doping (5.4 wt.%) for MPNC7 and MPNC23, respectively. In comparison, mainly carbon (98.3 wt.%) is found for KB, with only small amounts of heteroatoms (<1.2 wt.%) (Table S1, Supporting Information).

X-ray photoelectron spectroscopy (XPS) (Figure S5 and Table S2, Supporting Information) was performed to investigate the surface composition of the carbon supports, directly affecting the ionomer–carbon interaction and hence ionomer distribution on/in the derived electrocatalysts and CCMs.[19–21] In

S. Vierrath
Electrochemical Energy Systems
IMTEK-Department of Microsystems Engineering
University of Freiburg
Georges-Koehler-Allee 103, 79110 Freiburg, Germany
S. Vierrath, A. Fischer
Freiburg Center for Interactive Materials and Bioinspired Technologies (FIT)
University of Freiburg
Georges-Köhler-Allee 105, 79110 Freiburg, Germany
A. Fischer
Cluster of Excellence livMatS
University of Freiburg
79104 Freiburg, Germany

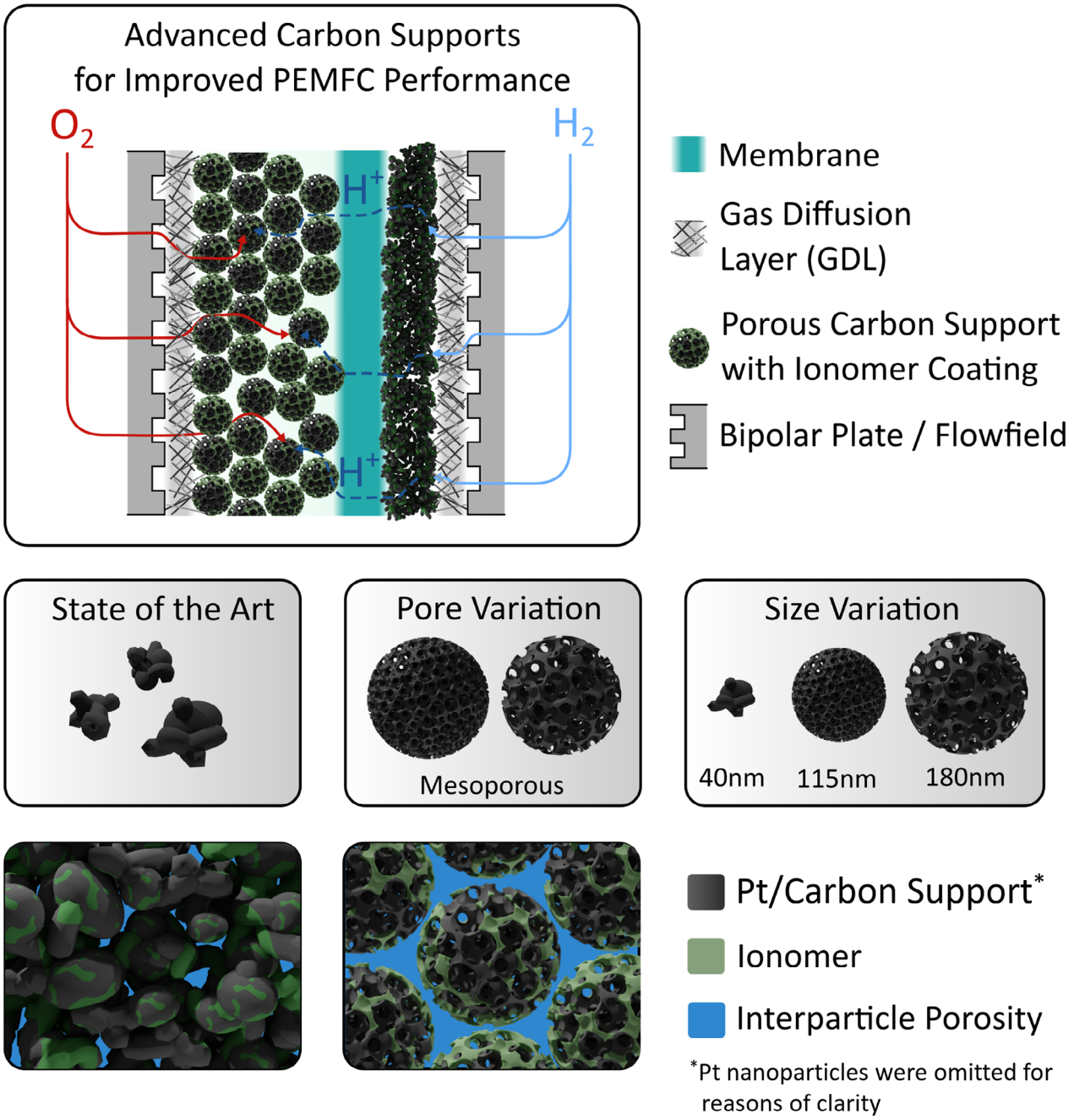

Figure 1. Schematic representation of a membrane electrode assembly (MEA) (top) with a catalyst-coated membrane (CCM) comprised of a Pt/MPNC catalyst, an ionomer in the catalyst layer (green) and a proton-conducting membrane (cyan). Morphology and particle size of state-of-the-art carbon supports (primary and secondary particles) versus monodisperse mesoporous N-doped carbon nanosphere support (MPNC) with tailored intraparticle (meso-)porosity (middle). CCM structure obtained with state-of-the-art Pt/C catalysts versus advanced MPNC supports derived Pt/MPNC catalysts enabling a 3D bottom-up CCM design with tailored intra- and interparticle porosity (bottom). Pt nanoparticles were omitted for reasons of clarity.

the MPNC nanospheres the N groups (Figure 2f) are mainly pyrrolic, along pyridinic, pyridonic/amine, quaternary/graphitic N, and NO_x groups; results, which are in line with our previous reports.[14]

The high heteroatom content relates to the broad defect (D, ≈1345 cm^{-1}) and graphitic (G, ≈1580 cm^{-1}) Raman bands. The D and G bands were deconvoluted into five bands, including four defect bands D1, D2, D3, D4, and one graphitic band G (Figure S6, Supporting Information). While the G band areas were comparable for MPNC7 and MPNC23 (17%), the KB showed a slightly increased G band area (21%) revealing a slightly more graphitic carbon microstructure. However, both carbon material types (MPNC and KB) can be classified as semi-crystalline as both Raman and X-ray diffraction (XRD)

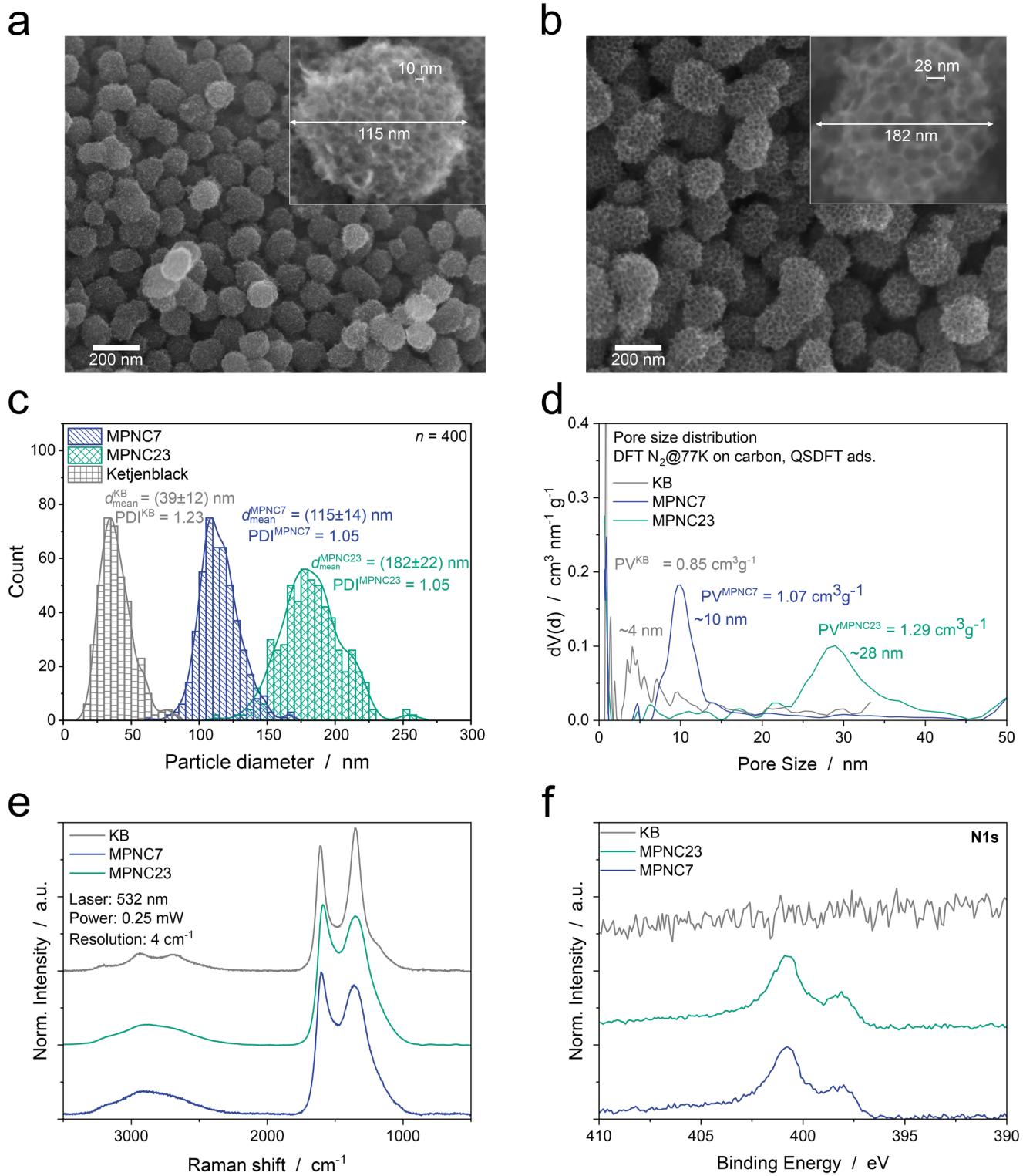

Figure 2. MPNC nanosphere characterization. SEM micrographs of the synthesized a) MPNC7 and b) MPNC23 along with their c) particle size distributions with mean particle diameters of 115 ± 14 nm and 182 ± 22 nm for MPNC7 and MPNC23, respectively, in comparison to 39 ± 12 nm for KB. d) QSDFT pore size distributions determined from N_2 physisorption experiments feature a pore size maximum around 10 and 28 nm for MPNC7 and MPNC23, respectively, while KB features a maximum around 4 nm. e) Raman microscopy of the carbon materials shows a slightly lower relative graphitization degree (Figure S6, Supporting Information) of the MPNC supports (G band integral area of 17%) compared to KB (21%). f) XPS N1s measurements reveal substantial N-doping only for the MPNCs supports, as verified by elemental analysis (Table S1, Supporting Information).

do not show sharp signals (Figure 2e,f; Figure S7, Supporting Information).

The dispersion behavior of the carbon materials was examined in a water/isopropanol mixture to reflect the conditions used in catalyst ink formulations and to evaluate dispersion stability under relevant processing conditions. Therefore, the measured zeta potentials were −(28.56 ± 1.11) mV for MPNC7, −(18.24 ± 0.17) mV for MPNC23, and −(40.81 ± 1.62) mV for KB (Figure S8, Supporting Information), indicating negatively charged surfaces and suggesting good colloidal stability as high absolute values suggest increased surface charges that result in a low degree of aggregation due to strong repulsive forces within the dispersion.[22]

Based on EA, XPS, Raman spectroscopy, and XRD the chemical and microstructural similarity of the MPNC supports (pore and particle size apart) was demonstrated, enabling to relate differences in the MPNC-based electrocatalysts and derived CCMs performance to differences in intra- and interparticle porosities (vide infra).

3. Pt/MPNC Catalyst and Cathodic Catalyst Layer (CCL) Characterization

To study the effect of the carbon support morphology/porosity on PEMFC performance, the same Pt deposition (know-how protected by Heraeus Precious Metals, not to be disclosed) was performed on the monodisperse MPNC nanosphere and the reference KB carbon supports with the aim to provide three catalysts with the same Pt species in terms of Pt nanoparticle size, distribution and wt.%. The Pt nanoparticles were homogeneously distributed on all carbon supports as revealed by transmission electron microscopy (TEM) (**Figure 3a–c**; Figure S9, Supporting Information) and have a size of ≈3 nm. Furthermore, the XRD measurements (Figure 3e) of the catalysts show almost identical Pt patterns, which proves identical Pt nanoparticle crystallinity and crystallite size (≈2.5 nm) of the Pt species. The obtained platinum loading (determined by TGA) on the different carbon supports is very similar in all cases and accounts for ≈50 wt.% (Figure 3d). XPS revealed the presence of Pt^0, Pt^{2+} und Pt^{4+} features in all cases, typical for Pt/C electrocatalysts, with only minimal differences between the electrocatalysts (Figure 3f; Figure S10 and Table S3, Supporting Information).

Nitrogen physisorption of the catalysts reveals that the specific surface area decreases in line with the increase in mass due to Pt deposition for all samples. For the MPNC samples, the data show that Pt deposition occurs without pore blocking and that the Pt nanoparticles are deposited within the mesopores, while for KB some pore blocking of micropores occurs (Figure S11, Supporting Information).

Electrochemical characterization in RDE configuration revealed a higher ECSA for MPNC-based materials and reflected an enhanced Pt nanoparticle dispersion on the MPNC nanospheres. This trend was not reflected in RDE mass activity measurements, with similar mass activities for all catalysts. In contrast at the MEA level differences related to morphology and porosity of the carbon supports on the activity and mass transport phenomena will be revealed (see below and Figures S12 and S13 and Table S4, Supporting Information).[2,23]

At the cathode, inks of Pt/MPNC7, Pt/MPNC23, and Pt/KB with an ionomer to carbon (I/C) weight ratio of 0.9 were spray-coated with a loading of 0.4 mg_{Pt} cm^{-2} onto a Nafion membrane (15 µm thickness, Fumatech GmbH), while at the anode 0.1 mg_{Pt} cm^{-2} of a Pt/C reference catalyst was deposited on the other side of the membrane. The resulting CCM was assembled into MEAs. From the SEM cross-section micrographs, one can see that the Pt/MPNC-derived cathode catalyst layers (CCL) exhibit a more open porous 3D structure, while the Pt/KB-derived CCLs reveal a more compact and denser 3D structure (**Figure 4**; Figure S14, Supporting Information). The resulting 3D structures of the CCLs are thereby in line with the primary particle size and morphology of the carbon supports, i.e., open porous 3D structures for MPNC with large primary particle sizes (Figure 4), in contrast to denser structures for Pt/KB with the smaller particle sizes. This result is very promising, as increasing the porosity of the catalytic layer may result in improvements in electrochemical performance at the MEA level, as demonstrated before in literature.[24,25]

4. 3D Porous Pt/MPNC Nanosphere Catalysts with Enhanced Fuel Cell Performance

All single cell measurements were performed with an active area of 12 cm^2 at 80 °C cell temperature and with flow rates of 2 l min^{-1} H_2 and 5 l min^{-1} air, if not otherwise stated. To confirm the reproducibility of the measurements, two MEAs were measured for each material and the mean value with standard deviation is shown in all graphs (Figure 5).

To demonstrate the potential of tailored MPNC nanospheres as advanced carbon supports for PEMFC CCLs, we characterized the Pt/MPNC23 catalyst compared to the reference material (Pt/KB) under different relative humidities (RH) and gas pressures (Figure 5a,b), and under typical conditions for heavy-duty applications of 50% relative humidity (RH) and ambient gas pressure (**Figure 5c**).[26] Remarkably, the Pt/MPNC23-based single-cell reaches a rated power density of 0.23 W cm^{-2} at 0.76 V and outperforms the Pt/KB with a power density of 0.17 W cm^{-2} by 30% (Figure 5d).[27] Electrochemical impedance spectroscopy (EIS) measurements under H_2/N_2 at a cell potential of 200 mV show the higher protonic conductivity for Pt/MPNC23 with a protonic resistance of 130 mΩ cm^{-2}, 40% lower than for the reference Pt/KB (222 mΩ cm^{-2}) (Figure 5e). The data was fitted using the EIS model described in Table S5 (Supporting Information). In Figure 5c the excellent performance at high current densities (>2 A cm^{-2}) of the Pt/MPNC23 material becomes apparent, which can be attributed to a substantially improved oxygen diffusion within the Pt/MPNC23 CCL, as corroborated by the local pressure-independent diffusion resistance of 3.7 s cm^{-1} measured with limiting current measurements,[26,28] which is five times lower than the one determined for the Pt/KB reference material CCL (20.5 s cm^{-1}) (Figure 5e). As presented before, the Pt/MPNC23 exhibits the highest mesopore volume and drastically improves gas diffusion through the mesopores under dry conditions. At higher RH above 95% the free pore space decreases due to full saturation of water inside the pores.[29] This full saturation means the gas diffusion in the intraparticle pores is determined only by Knudsen diffusion, which is favored for larger pores. Hence, the Pt/MPNC23 catalyst and derived CCL

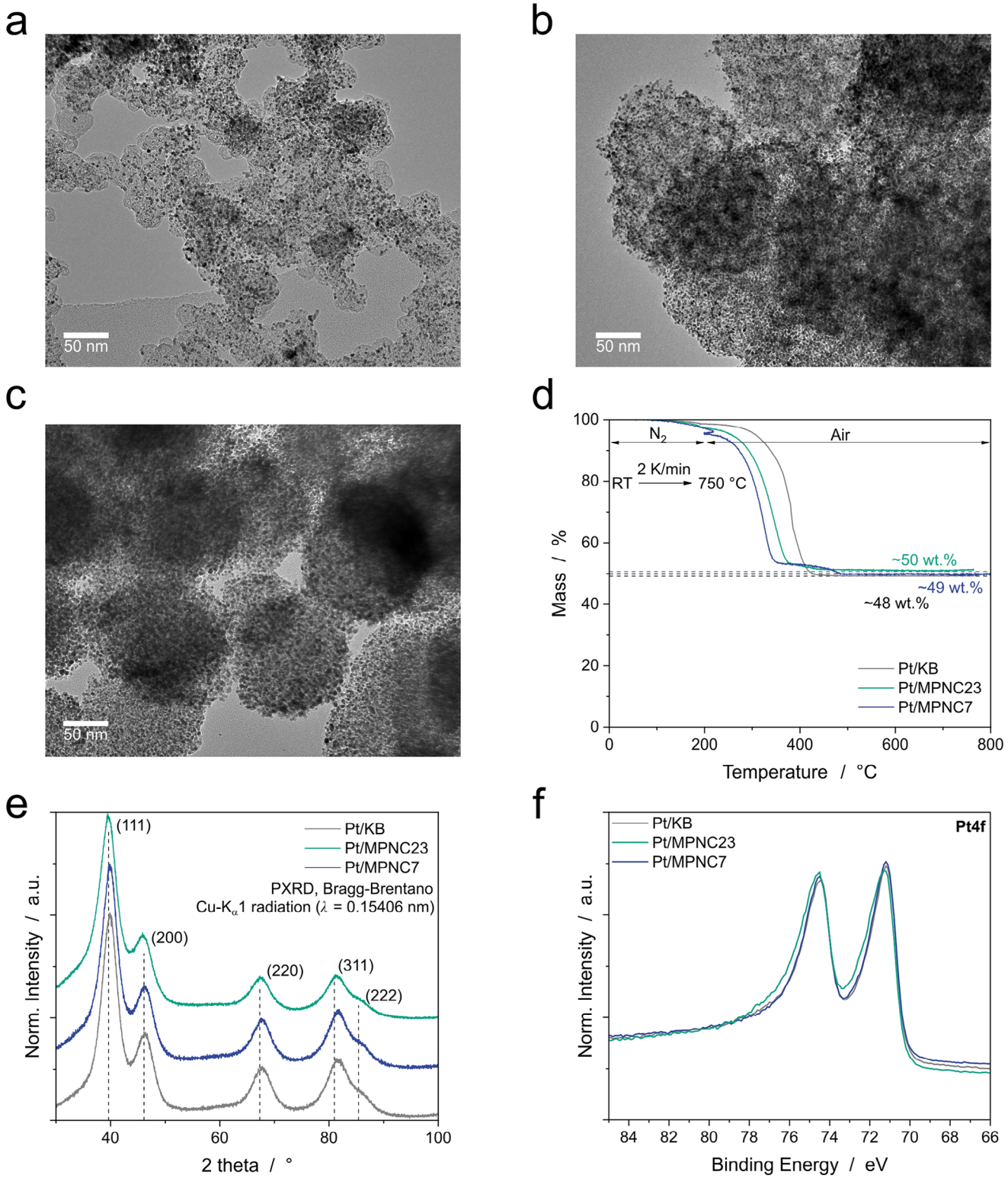

Figure 3. Pt/MPNC catalyst characterization. TEM micrographs of the synthesized a) Pt/KB, b) Pt/MPNC23, and c) Pt/MPNC7 catalysts show highly dispersed Pt nanoparticles on all carbon supports. Higher magnifications reveal very similar Pt nanoparticle sizes for all carbon supports (Figure S9, Supporting Information). Together with e) XRD data a comparable Pt nanoparticle/nanocrystallite size of ≈2.5 nm is confirmed for all carbon supports. The almost identical Pt mass loadings (between 48 and 50 wt.%) were determined by d) TGA. f) XPS measurements and Pt4f spectra confirm the presence of very similar Pt nanoparticles with very similar surface properties on all carbon supports.

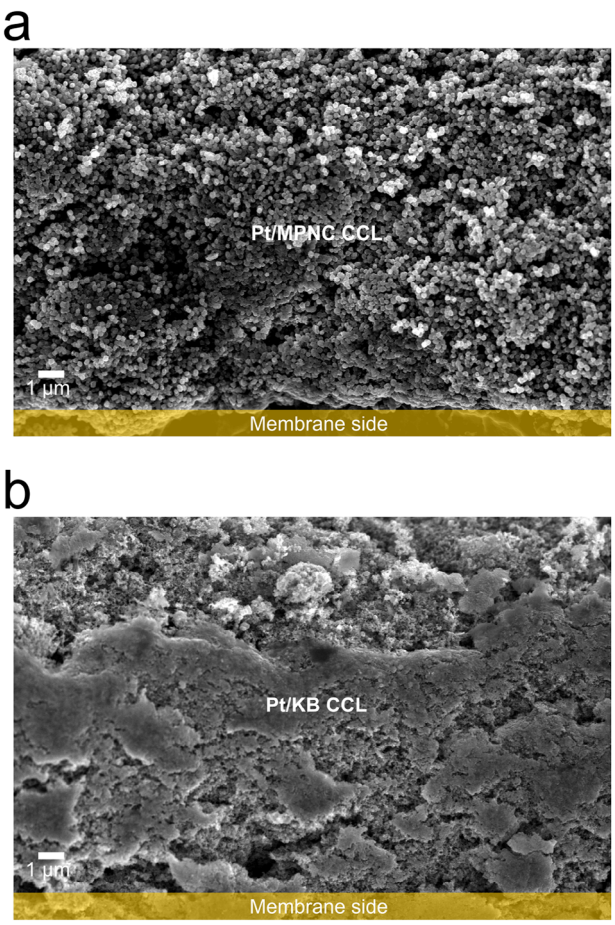

Figure 4. Cross-sections of prepared CCMs. The spray-coated CCL with an I/C ratio of 0.9 and a cathode loading of 0.4 mg_{Pt} cm^{-2} were investigated with SEM for the different catalysts, i.e., a) Pt/MPNC 23, Pt/MPNC7 (Figure S14, Supporting Information) and b) Pt/KB. For the Pt/MPNC CCLs a more open porous structure in line with the larger MPNC particle size (>100 nm) is found, in contrast to a denser structure in line with the smaller KB particles (<50 nm) for the Pt/KB.

combine two decisive aspects: improved performance under dry conditions due to good protonic conductivity and at the same time outstanding mass transport characteristics. These two aspects often contradict each other, since a good protonic conductivity and therefore high retention of water at low humidities can result in flooding at high humidities and oxygen mass transport limitations.[30] The designed MPNC23 particles and their pore structures enable the combination of both advantages, which gives us a glimpse into the potential of 3D porous carbon design for CL design and boosts MEA performance.

At a high RH of 100% the effect of good protonic conductivity is less relevant and higher activity losses in the Pt/MPNC23 CCL become apparent (Figure 5a, **Figure** 6a), as confirmed by mass activity (MA) measurements at 0.9 V (Figure 6c) revealing the smallest MA for the Pt/MPNC23 CCL (54.93 A g_{Pt}^{-1}) when compared to the Pt/KB CCL (67.51 A g_{Pt}^{-1}) and the Pt/MPNC7 CCL (69.31 A g_{Pt}^{-1}).

This trend is maintained under H_2/air in the voltage region relevant for automotive applications: with 0.66 W cm^{-2} at 0.76 V the Pt/MPNC7 outperforms both, the Pt/MPNC23 (0.52 W cm^{-2}) and the reference material Pt/KB (0.60 W cm^{-2}), by 26.9% and 10.0% respectively (Figure 6b). Besides the internal comparison in this work to the self-synthesized Pt/KB, in-depth comparison with literature results can be found in Figures S20–S24 (Supporting Information). The comparison of polarization curves obtained with catalysts made with tailored carbon supports (Figure S20, Supporting Information) confirms the outstanding performance of Pt/MPNC7 with a performance that reaches that of PtCo/C catalyst. The simplest explanation for the improvement of MA by reduction of pore size in the Pt/MPNC7 CCLs compared to Pt/MPNC23 CCLs, would be a reduction of the blockage of platinum surface by ionomer side chain end group ($-SO_3^-$) adsorption by hindering the intrusion of ionomer into the smaller pores, which in principle can be measured with CO displacement measurements.[9] For Pt/MPNC23 the higher activation loss (Figure 6d) aligns with CO displacement measurements that show that 16.5% of the Pt/MPNC23 ECSA is blocked by SO_3^- ionomer end groups, while only 14.0% of the ECSA is blocked for the Pt/KB ECSA. For the Pt/MPNC7 material, no distinct statement in this regard can be made (Figure 6d). Further, in-depth investigations are needed to explain the improved performance of Pt/MPNC7 in terms of ionomer catalyst interplay.

The MPNC nanosphere catalyst with a pore size of 10 nm (Pt/MPNC7) is not shown in Figure 5 for the sake of clarity. However, the data can be found in Supplementary Information (Figure S15, Supporting Information). With a power output of 0.25 W cm^{-2} at 0.76 V and under conditions of 50% RH and 100 kPa, the Pt/MPNC7 material outperforms the Pt/KB material by 47%.

One aspect that we investigated is the ionomer distribution on/in the carbon material. The CO capacitance method[10] uses carbon monoxide to mask the Pt nanoparticles and measures only the ionomer carbon double layer capacitance (DLC) under dry conditions (10% RH) and the total DLC at 100% RH, that summarizes the DLCs of ionomer and water in contact with carbon, designated as wettable carbon surface. At 100% RH, DLCs for Pt/MPNC23 (56 mF cm^{-2}) and Pt/MPNC7 (66 mF cm^{-2}) are approximately twice that of Pt/KB (29 mF cm^{-2}), hence a higher wettability of the MPNC is visible, despite the higher or comparable BET surface area of KB. The ratio of dry DLC over humid DLC defines the amount of wettable carbon surface covered by ionomer, which can be described as a relative ionomer coverage. The results in **Figure** 7a show that 43.7% of the wettable carbon surface is covered by ionomer for Pt/MPNC23, 41.9% for Pt/MPNC7, and only 37.5% for Pt/KB. This higher relative ionomer coverage on the MPNC materials can be attributed to two aspects: 1) the N-doping of the carbon is expected to lead to a more homogeneous ionomer coverage and 2) the bigger pore sizes could result in higher ionomer intrusion into the pores and MPNC particles.[5,20] Opposing to negative effects of this high ionomer coverage, like a higher ionomer side chain poisoning, is the fact that the MPNC-derived catalysts perform better than the reference KB-derived catalysts under dry conditions and at high current densities. It is assumed that this high distribution of ionomer for the MPNC materials leads to a thin homogenous ionomer film preferable for low oxygen transport resistances.[31] Besides the ionomer coverage

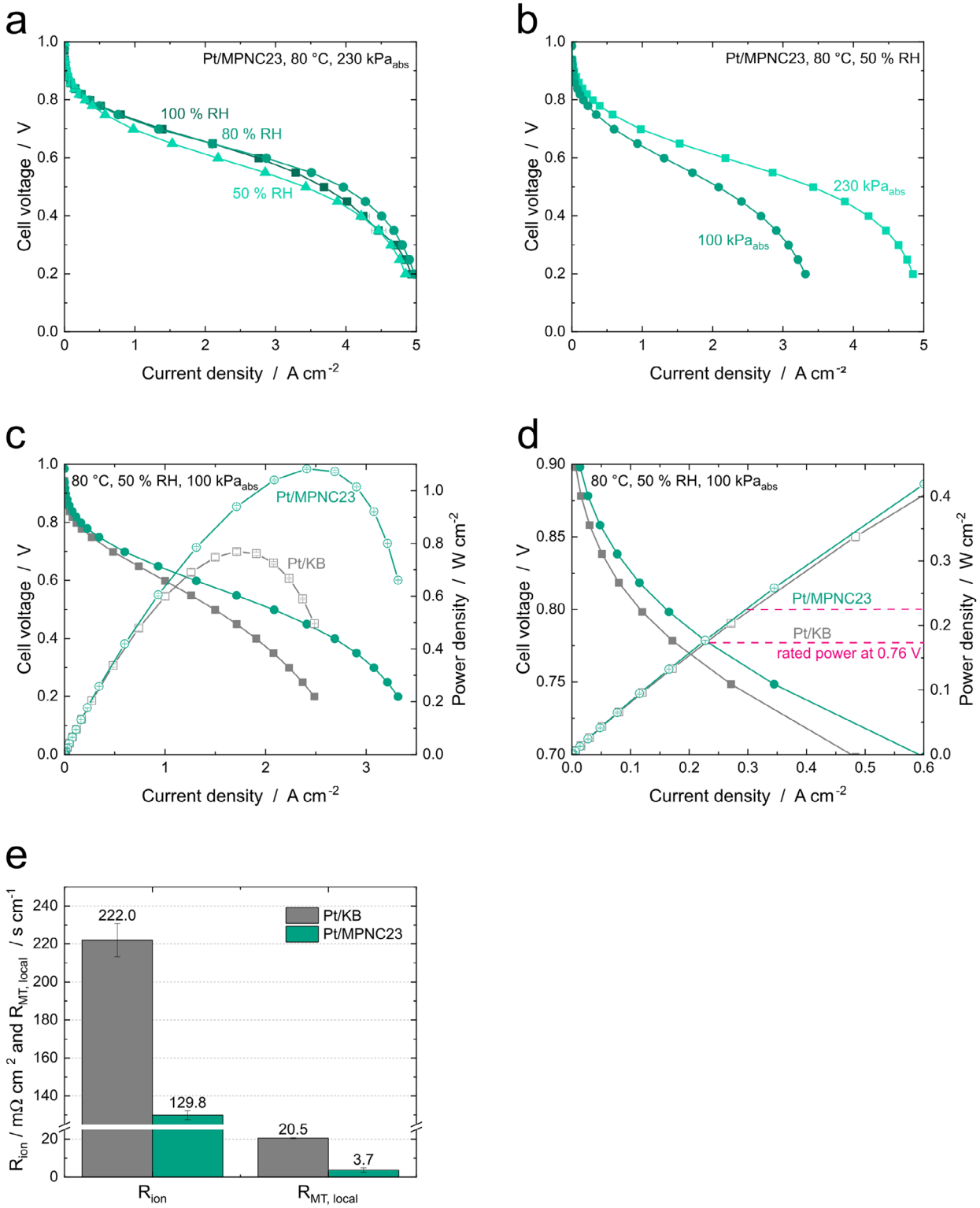

Figure 5. Single-cell fuel cell characterization of Pt/MPNC23 CCL and comparison to reference Pt/KB CCL. H_2/air polarization curves for Pt/MPNC23 CCL at a) 100, 80, and 50% relative humidities and b) two gas pressures. c) H_2/air polarization curves (filled symbols) and power densities (open symbols) for Pt/KB and Pt/MPNC23 CCL at 50% RH and 100 kPa$_{abs}$ d) and the associated inset with a dashed line to indicate rated power density of 0.23 W cm^{-2} (Pt/MPNC23) and 0.17 W cm^{-2} (Pt/KB). e) Protonic resistance (R_{ion}) calculated from EIS under H_2/N_2 for Pt/KB and Pt/MPNC23 CCL at 50% RH and 230 kPa$_{abs}$ and local pressure independent diffusion resistance ($R_{MT, local}$) for Pt/KB and Pt/MPNC23 CCL calculated with pressure independent diffusion resistance from limiting current measurement multiplied by roughness factor (measurements including Pt/MPNC7 are presented in the Figure S15, Supporting Information).

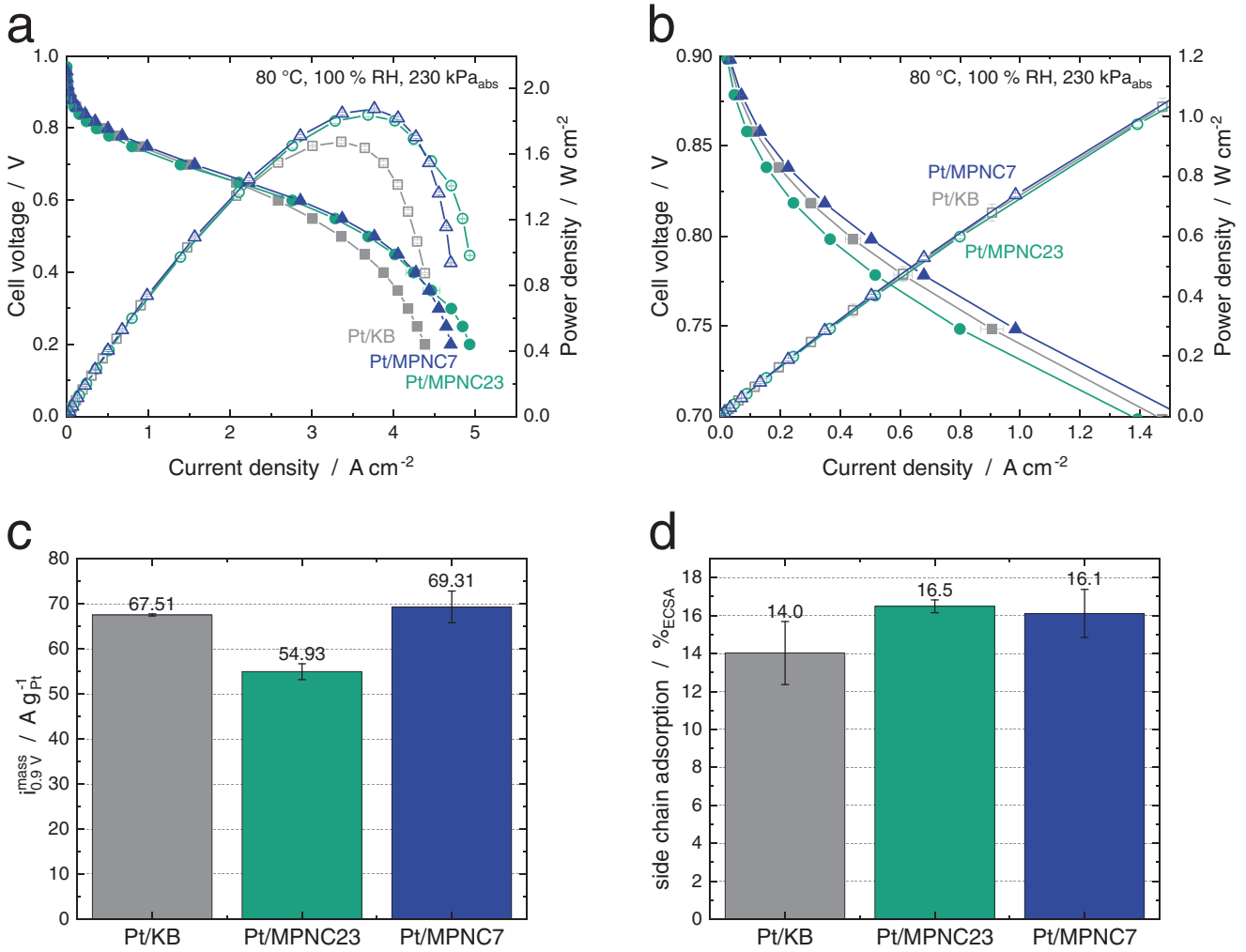

Figure 6. Performance of single-cell fuel cells comparing Pt/MPNC7, Pt/MPNC23, and Pt/KB reference CCLs. a) H_2/air polarization curves (filled symbols) and power densities (open symbols) for Pt/MPNC7, Pt/MPNC23 and Pt/KB at 100% RH and gas pressure of 230 kPa_{abs} and b) associated inset on heavy-duty relevant cell potential region. c) iR and H_2-crossover corrected mass activity measured under H_2/O_2 at 150 kPa_{abs} and d) percentage of ECSA blocked by ionomer side chains.

on carbon, the proton access to platinum is crucial for a full picture of the catalyst ionomer and water interplay that can be investigated with CO stripping. With this measurement under different RH, we can estimate the Pt in contact with ionomer ($ECSA_{Ionomer}$ at low RH) or water ($ECSA_{Water}$ as the difference between ECSA at high RH and ECSA at low RH) and the fraction of $ECSA_{Ionomer}$ to $ECSA_{total}$ (Figure 7b). In literature, this is described as dry proton accessibility (DPA).[4] The results show higher $ECSA_{Ionomer}$ for the MPNC materials of 43.4 $m^2\ g_{Pt}^{-1}$ for Pt/MPNC23 and 46.4 $m^2\ g_{Pt}^{-1}$ for Pt/MPNC7 compared to 37.0 $m^2\ g_{Pt}^{-1}$ for Pt/KB. These results underline the results of the CO capacitance and CO displacement measurements of a higher ionomer coverage on carbon and platinum for the MPNC materials. Regarding the ECSA under humid conditions, the Pt/MPNC23 (9.9 $m^2\ g_{Pt}^{-1}$) shows a smaller $ECSA_{Water}$ than Pt/KB (14.2 $m^2\ g_{Pt}^{-1}$) and Pt/MPNC7 (13.1 $m^2\ g_{Pt}^{-1}$). One explanation could be the pore size of 28 nm, which enables less water condensation, an assumption that must be confirmed by further investigations. The high $ECSA_{Water}$ of Pt/MPNC7 together with the high $ECSA_{Ionomer}$ leads to a DPA of 78% which is classified between the reference material Pt/KB (72% DPA) and the Pt/MPNC23 (82% DPA). This balance between a high ionomer coverage on the catalyst material and still high water-activated ECSA due to the good wettability of the Pt/MPNC7 results in high mass activity, good performance under dry conditions and still reaches high current densities due to good oxygen transport through the pore system. The work from Yarlagadda et al. showed the decrease of local O_2 resistance with increasing DPA but at the same time a reduction of MA due to higher accessibility of Pt for ionomer and hence higher blocked ECSA by ionomer side chains.[4] Our results show that Pt/MPNC7 material overcomes this trend with the increase in mass activity and performance with increasing ionomer coverage, which indicates a path towards an optimum pore size. Further investigations in the future on the effect of different pore and particle sizes in such Pt/MPNC catalysts are highly promising to further advance the understanding of the working mechanisms

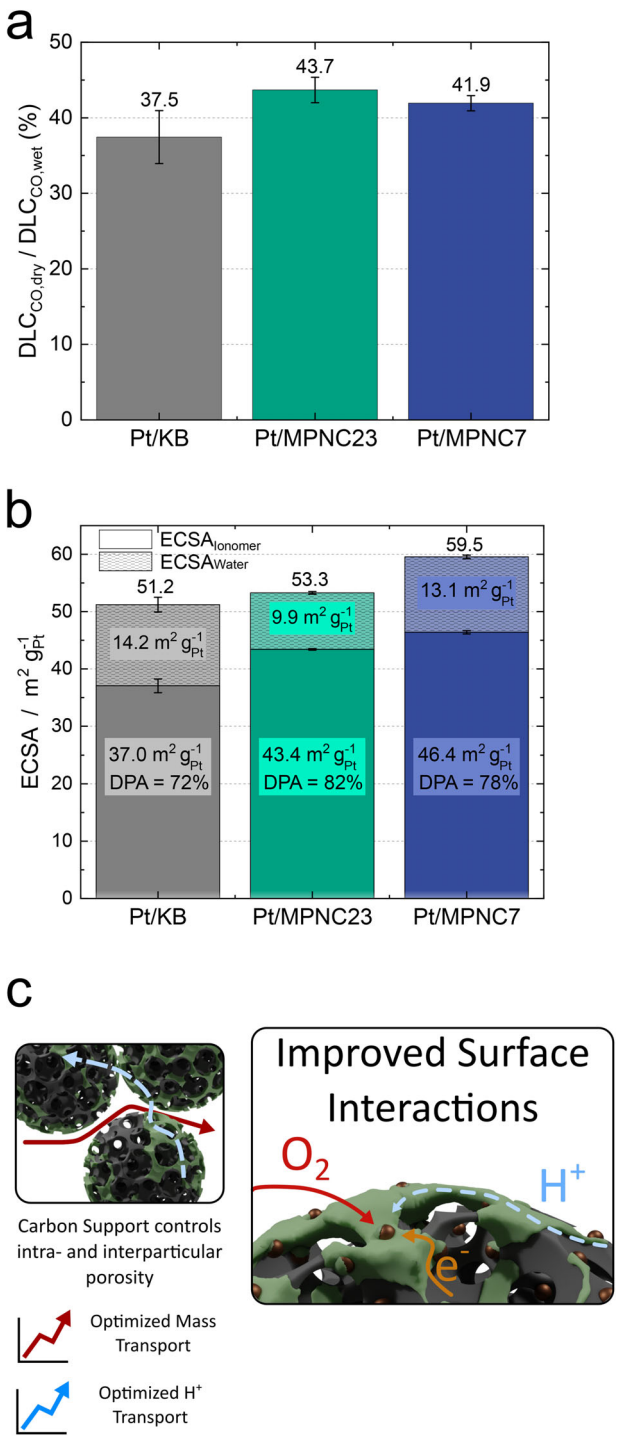

Figure 7. Ionomer coverage and distribution on Pt/carbon catalysts. a) Ionomer coverage of the total wettable surface measured with CO capacitance as the ratio of dry double layer capacitance (DLC) over humid DLC. b) ECSA measured by CO stripping at 20% RH ($ECSA_{Ionomer}$) and 100% RH ($ECSA_{total}$) and the difference between these ECSAs which describes the $ECSA_{Water}$. c) Schematic illustration displaying the improved surface interactions of ionomer and MPNC support as well as enhanced mass and proton transport through the MPNC-based CCM.

of mesoporous carbon supports in PEMFC catalyst and catalyst layer design.

The results lead to a hypothesis of ionomer distribution shown in Figure 7c for the three materials presented in this study. The reference Pt/KB material hides Pt inside smaller micro- and mesopores, where ionomer cannot reach it, but results also in a poorer ionomer distribution either by a poorly connected ionomer network on the outer surface of one carbon particle or by less intrusion of ionomer into the pores. The MPNC materials allow, with their bigger pores, an intrusion of ionomer into the intraparticle pores and a good protonic network over the whole carbon particle. Additionally, the good wettability of the MPNC material leads to high water-activated ECSA. The Pt/MPNC7 material adds to these factors a balanced pore size to particle size ratio and therefore, enhances a homogeneous and even ionomer distribution, leading to a higher protonic conductivity, excellent oxygen transport, and high performances over a wide range of conditions.

5. Conclusion

The potential of tailored 3D mesoporous N-doped carbon nanosphere (MPNC) supports and their effect on mass transport, protonic conductivity, and activity in PEMFCs are presented in this work. Two MPNC supports and thereof derived Pt/MPNC catalysts were synthesized, characterized, and compared to a Pt/KB reference material. Both MPNC derived catalysts and CCL show a high ionomer coverage and therefore a good protonic conductivity even under dry conditions. The larger pore size of 28 nm (Pt/MPNC23) leads to excellent local oxygen transport properties but an increased blocked ECSA by ionomer side chains and hence a lower mass activity. The smaller pore size of 10 nm (Pt/MPNC7) maintains the mass transport properties and additionally achieves an excellent mass activity with a combination of high ionomer coverage and water condensation inside the pores for a high ECSA. These improvements are reflected in the performance over a wide range of conditions. At 50% RH and 100 kPa gas pressure, the Pt/MPNC7 material achieves a performance of 0.25 W cm^{-2} at 0.76 V, and at 100% RH and 230 kPa, it reaches 0.66 W cm^{-2}, outperforming the reference material Pt/KB by 47% and 27%, respectively. In particular, the oxygen transport and the protonic conductivity are performance-determining factors here. This work paves the way for further increases in fuel cell performance through tailored carbon supports, which can achieve high power densities in all current density ranges under both dry and wet conditions.

6. Experimental Section

Chemicals and Reagents: Aniline ($C_6H_5NH_2$, VWR, Analar Normapur, ≥99.5%), colloidal SiO_2 (Sigma Aldrich, Ludox, 23 nm (34 wt.% in water) and 7 nm (30 wt.% in water) particle sizes), ethanol absolute (C_2H_5OH, VWR, 99.5%), isopropanol absolute (C_3H_7OH, HPLC grade, 99.9%) ammonium persulfate ($(NH_4)_2S_2O_8$, APS, Sigma Aldrich, ≥98.0%) were directly used without further purification. Ammonium hydrogen fluoride (NH_4HF_2, ≥98%) was dissolved in water to obtain a concentration of 4 M. 5 M HCl (Fisher Scientific, 5 M) was diluted with water to prepare 1 M HCl. For the electrochemical ORR catalyst and fuel cell tests perchloric acid ($HClO_4$, Sigma Aldrich, 70% trace metal basis),

a PFSA ionomer 800EW (3 M), a gas diffusion layer (GDL, Freudenberg H23C9) and a fumapem membrane (FS715RFS, 715EW, 15 µm, Fumatech) were purchased. The reference carbon support Ketjenblack EC-300J (KB) was provided by Nouryon and the commercial Pt/C catalyst (46.4 wt.%, TEC10E50E), used as anode, was purchased from TKK.

Synthesis of Mesoporous N-Doped Carbon Nanospheres and Pt Depositions: Details of the synthesis of MPNC nanospheres are reported elsewhere.[12–16,32,33] In brief, 94 mmol L^{-1} aniline and SiO_2 nanoparticles (11.8 g L^{-1} MPNC23; 10.3 g L^{-1} MPNC7) are dispersed in 0.1 M HCl (3375 mL) and cooled in an ice bath. Subsequently, 2.2 mol L^{-1} of APS dissolved in 1 M HCl (150 mL) solution is added dropwise to the reaction mixture under vigorous stirring for 24 h in an ice bath. The resulting composite PANI/SiO_2 material is washed with water until the supernatant is neutral and freeze-dried. The dry product is carbonized in a tube furnace at 1000 °C for 6 h using a heat ramp of 200 °C h^{-1}. MPNC/SiO_2 material is treated with an ammonium hydrogen fluoride solution (4 M, 50 mL g^{-1} of MPNC/SiO_2, 48 h) to remove the SiO_2 template and subsequently washed to pH neutrality. The resulting MPNC material is transferred to ethanol, stirred for 24 h, and dried in air. Finally, the MPNC product was heat treated at 500 °C for 2 h under N_2 atmosphere. For the preparation of the catalyst, a Pt deposition - proprietary to Heraeus - was applied on the MPNC nanospheres and commercial KB carbon support, aiming for a Pt loading of 50 wt.%.

Physical Characterization: Morphological analysis was performed by SEM (Hitachi, FEG HRSEM SU8220) and TEM (the latter by Heraeus). The carbon microstructure and Pt nanoparticles of Pt/MPNC and Pt/KB were examined with a X-ray diffractometer (Bruker D8) equipped with a Cu Kα radiation source. Bulk and surface compositions were evaluated through elemental analysis (Elementar Analysensysteme GmbH, Vario MICRO Cube System) and X-ray photoelectron spectroscopy (SPECS, EnviroESCA), respectively. Furthermore, Pt loading was determined by thermogravimetric analysis (Netzsch Gerätebau GmbH, STA449 F5). N_2 physisorption isotherms were processed by the Brunauer–Emmett–Teller method and a quenched solid density function theory kernel (3P, 300Mikro, QSDFT QuadraWin, Quantachrome) to evaluate the surface area, pore volume and pore size distribution. Microstructural analysis was performed by Raman spectroscopy (Bruker Optics GmbH, Senterra II Raman microscope). Zeta potential measurements were conducted using a Litesizer 500 (Anton Paar). For each carbon sample, 2 mg of carbon were dispersed in 2320 µL of water and 730 µL of isopropanol and homogenized with an ultrasonic horn (Branson 150) for 30 min under ice cooling using a pulse program (3 on and 2 s off). For the measurement, the samples were diluted 1:10 (m/m) in water/IPA mixture. Measurements were repeated at least three times.

Electrochemical Characterization: A Gamry Interface 1010E potentiostat was used for electrochemical rotating disc electrode (RDE) testing. All measurements shown were corrected by the uncompensated resistance R_u. The electrochemical ORR activity tests and CO stripping experiments were performed in a temperature-controlled homemade three-electrode cell. In this cell, the compartments of the counter electrode and the reference electrode were separated from the working electrode by a glass frit and a Luggin capillary, respectively. The temperature was kept at 25 °C throughout the entire experiment. Then, the catalysts were coated on a glassy carbon RDE (0.196 cm^2, Ametek) and used as a working electrode, whereas a reversible hydrogen electrode (RHE, Gaskatel Germany) and a Pt mesh (12 cm^2) were used as a reference and counter electrode, respectively. Catalyst inks were prepared by dispersing a specific amount of catalyst in 2320 µL of water, 730 µL of isopropanol, and a specific volume of ionomer dispersion (5 wt.% in isopropanol), to obtain a Pt electrode loading of 20 μg_{Pt} cm_{geo}^{-2} with an ionomer to carbon (I/C) weight ratio of 0.6. The inks were homogenized with an ultrasonic horn (Branson 150) for 15 min under ice cooling using a pulse program (3 s on and 2 s off). 10 µl of the catalyst ink was drop cast onto the GC part of the RDE and subsequently dried in air under rotation at 700 rpm. All electrochemical tests were conducted with freshly prepared (65 mL) 0.1 M $HClO_4$, the respective gas saturations following the same testing protocol. Initially, the catalysts were conditioned between 0.05 and 1 V versus RHE with 100 mV s^{-1} under N_2 saturation for 50 cycles, followed by 3 cyclic voltammograms with 20 mV s^{-1} in the same potential range. The third cycle allowed the determination of the electrochemical active surface area (ECSA) using the charge integral of the H_{upd} adsorption area and a theoretical charge density of 210 µC cm_{Pt}^{-2} of adsorbed hydrogen.[34] Subsequently, anodic linear sweep voltammetry curves between 0.05 and 1.1 V versus RHE under N_2 and O_2 saturation were recorded to determine the ORR activity at 0.9 V versus RHE.[34] Prior to LSV curves, a potential hold of 30 s at 0.05 V versus RHE was applied to ensure a comparable Pt surface for each measurement. Then, the electrolyte was purged with CO gas for 5 min, followed by a chronoamperometry with an electrode polarization of 0.1 V versus RHE for 10 min. During the first 2 min, the measurement was performed with a small CO flow followed by a consequent 8 min flow of N_2 to expel dissolved CO of the electrolyte. The subsequent CV curve was initialized at 0.1 V and cycled up to 1.25 V versus RHE to oxidize Pt-adsorbed CO. The generated charge of CO oxidation was integrated and subtracted by the charge observed during the 2nd cycle (0.05–1.25 V vs RHE) with the same integration limits.

CCM Fabrication: The Pt/MPNC and Pt/KB were used as cathode electrocatalysts and deposited on a PEM. 100 mg of electrocatalyst was homogenized in 4.97 g of distilled water, 1.24 g of isopropanol, and a specific amount of ionomer dispersion (5 wt.% in isopropanol), to achieve an ionomer (3 M Ionomer 800EW) to carbon weight ratio (I/C) of 0.9. The catalyst ink was dispersed for 60 min in an ice bath with a tip sonicator (Hielscher UIS250L) at 480 W. The mixed ink was sprayed centrally through an N_2-driven 60 kHz nozzle (Sonaer Sono Cell) onto the membrane (5 × 6 cm, Fumapem FS 715 RFS with 15 µm thickness from fumatech GmbH) covered by a 4 × 5 cm mask. The assembly was placed on an 80 °C hot plate until the dry CCM with a cell area of 20 cm^2 and a targeted cathode mass loading of 0.4 mg_{Pt} cm^{-2} (as determined gravimetrically and by micro-X-ray fluorescence (M4 Tornado of Bruker Nano GmbH)) was obtained. The anode electrocatalysts with a targeted mass loading of 0.1 mg_{Pt} cm^{-2} were sprayed on the other side of the membrane by using the same fabrication process but using the following ink recipe: 400 mg of TKK were dispersed in 19.89 g of distilled water, 4.97 g of isopropanol and 3.11 g of ionomer dispersion (5 wt.% in isopropanol) to obtain an I/C ratio of 0.73.

Single-Cell Test: The sprayed CCM was laminated into a frame with a window to ensure the exact active area of 12 cm^2. The CCM was assembled on both sides with gas diffusion layers with microporous layers (H23C9 Freudenberg GmbH) and included into the Baltic FuelCells quick-Connect liquid cooling cell with a graphite flow field with straight channels at a clamping pressure of 1.35 N mm^{-2} that was dynamically adjusted to the gas pressure. The single cell was connected to a fuel cell test bench designed and built in-house and electrochemically characterized using a potentiostat (Zennium Pro of Zahner-Elektrik GmbH & Co. KG) and an electronic load (PLI 1206ZV of Höcherl & Hackl GmbH). The cell temperature was controlled with a cryostat (ECO RE 1050 G of Lauda GmbH & Co. KG). The relative humidity (RH) of the gases was adjusted by leading the gases through humidifiers at a controlled temperature and mixing the humidified gases with a dry gas feed.

The MEA was activated under 100% RH at 80 °C cell temperature with 2/5 normal liter min^{-1} (NLPM) H_2/air and a gas pressure of 200 kPa_{abs} for 2 h at 1.5 A cm^{-2} following a recovery[35] and a potentiostatic cycling step for six hours at OCV (10 s), 0.6 V (60 s) and 0.4 V (60 s). The electrochemical characterization was performed in the following steps: 1) activity measurements, 2) polarization curves, 3) electrochemical impedance spectroscopy, 4) EIS under H_2/N_2, 5) CO displacement, 6) CO capacitance, 7) CO stripping, 8) limiting current measurement. The details of the characterization methods are described in the following sections.

Activity Measurements: The mass activity was measured under H_2/O_2 with 2 and 5 NLPM respectively, at 80 °C cell temperature, 150 kPa_{abs} gas pressure, and 100% relative humidity (RH) of the gases. The cell potential was operated between 0.88 and 0.92 V and after a conditioning period of 600 s the corresponding current was averaged over 60 s. The HFR was measured at 0.1 A cm^{-2} and the H_2 crossover with cyclic voltammetry measurement (1/0 NLPM H_2/N_2, 80 °C, 100 kPa_{abs}, sweep with 100 mV s^{-1} from 0.05 to 0.95 V) for HFR and H_2 crossover correction.

The corresponding current density at 0.9 V was divided by the Pt loading of the cathode catalyst layer.

Polarization Curves: Polarization curves were measured at H_2/air (with 2 and 5 NLPM respectively), 80 °C cell temperature, 100 and 230 kPa_{abs} gas pressure, and 100%, 80%, and 50% relative gas humidity. The cell current was measured at distinct potentials between OCV and 0.2 V. At a steady state (minimum of 5 min at certain cell potential and current variation below 1%) the cell current was averaged over 30 s.

Electrochemical Impedance Spectroscopy: For the EIS measurement, the cell was operated at 80 °C cell temperature and gas pressures of 230 kPa_{abs} under H_2/N_2 (1 and 1 NLPM). The EIS spectra were recorded at 200 mV with an amplitude of 10 mV at frequencies between 10000 Hz and 1 Hz. The resulting impedance spectra were evaluated with a transmission line model[36,37] including a constant phase element (CPE), protonic catalyst layer resistance R_{ion}, high-frequency resistance HFR, and hardware inductivity L. The model is described in Table S5 (Supporting Information).

CO Displacement: The aim of the CO displacement method is to measure the amount of SO_3^- side chain end groups blocking Platinum particles. The cell is operated at 40 °C cell temperature, with a relative humidity of 75% and at ambient pressure. A recovery protocol[35] and several potential cycles are performed to remove any volatile contaminants since the method is interested in stable contaminants. The cell potential is held at a potential of 0.3 V under diluted (10%) H_2 in N_2 on the anode and N_2 on the cathode side (2/2 NLPM). After 60 s 1 NLPM of 0.1% CO in N_2 is introduced to the cell. The integral of the accruing current peak (Q_{Disp}) is calculated. A following CO stripping reveals the available ECSA and the charge (Q_{Strip}).[9] The blocked ECSA at this certain potential is the ratio of:

$$(Blocked\ ECSA) = \frac{Q_{Disp}}{2 \times Q_{Strip}} \quad (1)$$

CO Capacitance: CO capacitance measurements were performed at a cell temperature of 40 °C and ambient pressure. The cell was operated at 200 mV under diluted (10%) H_2 in N_2 (2 NLPM) and 2 NLPM of 0.1% CO in N_2 for 20 min. The CO masks Pt sites and excess CO was flushed out with 2 NLPM N_2. Cyclic voltammetry measurements were performed by cycling the potential between 0.15 and 0.25 V to calculate the double layer capacity at 10% RH and at 100% RH. The potential is chosen to prevent any removal of CO by oxidation.[8,10]

CO Stripping: CO stripping measurements were performed at a cell temperature of 80 °C and ambient pressure. The cell was operated at 200 mV under diluted (10%) H_2 in N_2 (2 NLPM) and 2 NLPM of 0.1% CO in N_2 for 20 min. The CO masks Pt-sites and excess CO were flushed out with 2 NLPM N_2. Cyclic voltammetry measurements were performed by cycling the potential between 0.1 and 0.95 V. The CO was oxidized, and the revealing CO stripping peak was integrated to calculate the stripping charge. The $ECSA_{CO}$ was calculated with an assumed charge density of 420 μC cm_{Pt}^{-2}.[38] The method uses the reaction mechanism that CO is oxidized by water. At low hydration (20% RH) mainly ionomer retains water hence CO covering platinum that is in contact with ionomer is oxidized, while at higher hydrations CO covering platinum that is in contact with both, ionomer and water, is oxidized.

Limiting Current Measurement: Limiting current measurements were measured at 80 °C cell temperature and 100% relative gas humidity. The limiting current was calculated when regulating the cell potential from 0.60 to 0.15 V, at diluted oxygen concentrations of 1, 1.5, 2, and 2.5%, and gas pressures of 150, 200, 250, and 300 kPa_{abs}. The total resistance was averaged from all concentrations in each pressure level and divided into a pressure-dependent oxygen diffusion resistance and pressure-independent oxygen diffusion resistance.[27]

Supporting Information

Supporting Information is available from the Wiley Online Library or from the author.

Acknowledgements

This work was financially supported by the German Federal Ministry of Education and Research (BMBF, CORAL-HD, FKZ: 03SF0614A, 03SF0614B, 03SF0614C, 03SF0614D) as well as by core funding of the University of Freiburg. Jan Oechsler is acknowledged for help with the schematic illustration of the electrode (Figures 1 and 7c). Zohreh Kiaee is acknowledged for the help with the zeta potential measurements.

Conflict of Interest

The authors declare no conflict of interest.

Author Contributions

J.M., S.K., and K.C. contributed equally as the first authors to this work. A.F. initiated the research, planned the study and the experiments, supervised S.K., J.M., and P.E., and designed, coordinated, and edited the manuscript. J.M. and S.K. performed the MPNC support synthesis, the support and catalyst material characterization, and the RDE investigations, analyzed the corresponding data, and wrote the material synthesis and characterization part of the manuscript under the supervision of A.F. P.E. performed HRSEM and EDX measurements under the supervision of A.F. R.M. as part of Heraeus provided the catalysts and the TEM images. M.H. and H.F. prepared CCMs for the fuel cell study under the supervision of S.V. K.C. carried out all fuel cell measurements under the supervision of N.Z., analyzed all fuel cell-related data, and wrote the fuel cell part of the manuscript. K.A.F. supervised K.C. and edited the manuscript. J.M., S.K., K.C., R.M., M.H., H.F., S.V., N.Z., and A.F. discussed the results during the study and all authors read, commented, edited, and agreed on the manuscript.

Data Availability Statement

The data that support the findings of this study are available from the corresponding author upon reasonable request.

Keywords

carbon support, catalyst layer design, mass transport, mesoporous N-doped carbon nanospheres (MPNC), oxygen reduction reaction (ORR), proton exchange membrane fuel cells

Received: February 17, 2025
Revised: May 31, 2025
Published online: August 14, 2025

[1] U. S. Department of Energy, U. S. National Clean Hydrogen Strategy, and Roadmap 2023, https://www.hydrogen.energy.gov/docs/hydrogenprogramlibraries/pdfs/us-national-clean-hydrogen-strategy-roadmap.pdf?sfvrsn=c425b44f_5, (accessed: May 2025).
[2] J. Fan, M. Chen, Z. Zhao, Z. Zhang, S. Ye, S. Xu, H. Wang, H. Li, *Nat. Energy* **2021**, *6*, 475.
[3] T. A. M. Suter, K. Smith, J. Hack, L. Rasha, Z. Rana, M. Angel, P. R. Shearing, T. S. Miller, D. J. L. Brett, *Adv. Energy Mater.* **2021**, *11*, 2101025.
[4] V. Yarlagadda, M. K. Carpenter, T. E. Moylan, R. S. Kukreja, R. Koestner, W. Gu, L. Thompson, A. Kongkanand, *ACS Energy Lett.* **2018**, *3*, 618.
[5] S. Ott, A. Orfanidi, H. Schmies, B. Anke, H. N. Nong, J. Hübner, U. Gernert, M. Gliech, M. Lerch, P. Strasser, *Nat. Mater.* **2020**, *19*, 77.

[6] M. N. Islam, A. B. Mansoor Basha, V. O. Kollath, A. P. Soleymani, J. Jankovic, K. Karan, *Nat. Comm.* **2022**, *13*, 6157.
[7] S. Ott, A. Bauer, F. Du, T. A. Dao, M. Klingenhof, A. Orfanidi, P. Strasser, *ChemCatChem* **2021**, *13*, 4759.
[8] H. Iden, A. Ohma, *J. Electroanal. Chem.* **2013**, *693*, 34.
[9] T. R. Garrick, T. E. Moylan, V. Yarlagadda, A. Kongkanand, *J. Electrochem. Soc.* **2017**, *164*, F60.
[10] T. Van Cleve, S. Khandavalli, A. Chowdhury, S. Medina, S. Pylypenko, M. Wang, K. L. More, N. Kariuki, D. J. Myers, A. Z. Weber, S. A. Mauger, M. Ulsh, K. C. Neyerlin, *ACS Appl. Mater. Interfaces* **2019**, *11*, 46953.
[11] G. Wang, G. Sun, Q. Wang, S. Wang, H. Sun, Q. Xin, *Int. J. Hydrogen Energy* **2010**, *35*, 11245.
[12] T. Berestok, C. Diestel, N. Ortlieb, S. W. Glunz, A. Fischer, *Adv. Mater. Technol.* **2022**, *7*, 2200237.
[13] T. Berestok, C. Diestel, N. Ortlieb, J. Buettner, J. Matthews, P. S. C. Schulze, J. C. Goldschmidt, S. W. Glunz, A. Fischer, *Sol. RRL* **2021**, *5*, 2100662.
[14] S. Küspert, I. E. Campbell, Z. Zeng, S. E. Balaghi, N. Ortlieb, R. Thomann, M. Knäbbeler-Buß, C. S. Allen, S. E. Mohney, A. Fischer, *Small* **2024**, *20*, 2311260.
[15] N. Ortlieb, T. Berestok, P. Elsässer, R. Thomann, M. Knäbbeler-Buß, A. Fischer, *Small* **2024**, *21*, 2407235.
[16] J. Melke, R. Schuster, S. Möbus, T. Jurzinsky, P. Elsässer, A. Heilemann, A. Fischer, *Carbon* **2019**, *146*, 44.
[17] S. Slomkowski, J. V. Alemán, R. G. Gilbert, M. Hess, K. Horie, R. G. Jones, P. Kubisa, I. Meisel, W. Mormann, S. Penczek, R. F. T. Stepto, *Pure Appl. Chem.* **2011**, *83*, 2229.
[18] K. S. W. Sing, *Pure Appl. Chem.* **1985**, *57*, 603.
[19] Z. Fang, M. S. Lee, J. Y. Kim, J. H. Kim, T. F. Fuller, *J. Electrochem. Soc.* **2020**, *167*, 064506.
[20] S. Kabir, K. Artyushkova, A. Serov, P. Atanassov, *ACS Appl. Mater. Interfaces* **2018**, *10*, 11623.
[21] S. Ott, F. Du, M. L. Luna, T. A. Dao, B. R. Cuenya, A. Orfanidi, P. Strasser, *J. Electrochem. Soc.* **2022**, *169*, 054520.
[22] Y. Zhang, A. Narayanan, F. Mugele, M. A. C. Stuart, M. H. G. Duits, *Colloids Surf. A Physicochem. Eng. As.* **2016**, *489*, 461.
[23] T. Lazaridis, B. M. Stühmeier, H. A. Gasteiger, H. A. El-Sayed, *Nat. Catal.* **2022**, *5*, 363.
[24] J. Zhao, H. Liu, X. Li, *Electrochem. Energy Rev.* **2023**, *6*, 13.
[25] Z. Ni, L. Wang, B. Wang, *Int. J. Hydrogen Energy* **2024**, *60*, 1404.
[26] U. Beuscher, *J. Electrochem. Soc* **2006**, *153*, 1788.
[27] US Department of Energy, DoE Technical Targets PEMFC components, https://www.energy.gov/eere/fuelcells/doe-technical-targets-polymer-electrolyte-membrane-fuel-cell-components, (accessed: May 2025).
[28] D. R. Baker, D. A. Caulk, K. C. Neyerlin, M. W. Murphy, *J. Electrochem. Soc.* **2009**, *156*, B991.
[29] C. Strangfeld, *Adv. Eng. Mater.* **2021**, *23*, 2100106.
[30] R. Alink, R. Singh, P. Schneider, K. Christmann, J. Schall, R. Keding, N. Zamel, *Molecules* **2020**, *25*, 1523.
[31] R. Jinnouchi, K. Kudo, K. Kodama, N. Kitano, T. Suzuki, S. Minami, K. Shinozaki, N. Hasegawa, A. Shinohara, *Nat. Commun.* **2021**, *12*, 4956.
[32] Z. Zeng, S. Küspert, S. E. Balaghi, H. E. M. Hussein, N. Ortlieb, M. Knäbbeler-Buß, P. Hügenell, S. Pollitt, N. Hug, J. Melke, A. Fischer, *Small* **2023**, *19*, 2205885.
[33] J. Melke, J. Martin, M. Bruns, P. Hügenell, A. Schökel, S. Montoya Isaza, F. Fink, P. Elsasser, A. Fischer, *ACS Appl. Energy Mater.* **2020**, *3*, 11627.
[34] K. Shinozaki, J. W. Zack, R. M. Richards, B. S. Pivovar, S. S. Kocha, *J. Electrochem. Soc.* **2015**, *162*, F1144.
[35] United States Driving Research and Innovation for Vehicle Efficiency and Energy Sustainability (U.S. DRIVE) Partnership, Fuel Cell Technical Team Roadmap, 2017, http://energy.gov/eere/vehicles/downloads/us-drive-fuel-cell-technical-team-roadmap, (accessed: May 2025).
[36] R. Makharia, M. F. Mathias, D. R. Baker, *J. Electrochem. Soc.* **2005**, *152*, A970.
[37] D. Malevich, B. R. Jayasankar, E. Halliop, J. G. Pharoah, B. A. Peppley, K. Karan, *J. Electrochem. Soc.* **2012**, *159*, F888.
[38] E. Padgett, N. Andrejevic, Z. Liu, A. Kongkanand, W. Gu, K. Moriyama, Y. Jiang, S. Kumaraguru, T. E. Moylan, R. Kukreja, D. A. Muller, *J. Electrochem. Soc.* **2018**, *165*, F173.